SANDIA REPORT
SAND2001-0132
Unlimited Release
Printed February 2001

Modeling Error and Adaptivity in Nonlinear Continuum Mechanics

Daniel C. Hammerand, J. Tinsley Oden, Serge Prudhomme and Mieczyslaw S. Kuczma

Prepared by
Sandia National Laboratories
Albuquerque, New Mexico 87185 and Livermore, California 94550

Sandia is a multiprogram laboratory operated by Sandia Corporation, a Lockheed Martin Company, for the United States Department of Energy under Contract DE-AC04-94AL85000.

Issued by Sandia National Laboratories, operated for the United States Department of Energy by Sandia Corporation.

Available to DOE and DOE contractors from
U.S. Department of Energy
Office of Scientific and Technical Information
P.O. Box 62
Oak Ridge, TN 37831

Telephone: (865)576-8401
Facsimile: (865)576-5728
E-Mail: reports@adonis.osti.gov
Online ordering: http://www.doe.gov/bridge

Available to the public from
U.S. Department of Commerce
National Technical Information Service
5285 Port Royal Rd
Springfield, VA 22161

Telephone: (800)553-6847
Facsimile: (703)605-6900
E-Mail: orders@ntis.fedworld.gov
Online order: http://www.ntis.gov/ordering.htm

SAND2001-0132
Unlimited Release
Printed February 2001

Modeling Error and Adaptivity in Nonlinear Continuum Mechanics

Daniel C. Hammerand
Material Mechanics
Sandia National Laboratories
P.O. Box 5800
Albuquerque, NM 87185-0847

J. Tinsley Oden and Serge Prudhomme
Texas Institute for Computational and Applied Mechanics
The University of Texas at Austin
Austin, TX 78712

Mieczyslaw S. Kuczma
Poznan University of Technology
60-965 Poznan, Poland

Abstract

In this report, computable global bounds on errors due to the use of various mathematical models of physical phenomena are derived. The procedure involves identifying a so-called fine model among a class of models of certain events and then using that model as a datum with respect to which coarser models can be compared. The error inherent in a coarse model, compared to the fine datum, can be bounded by residual functionals unambiguously defined by solutions of the coarse model. Whenever there exist hierarchical classes of models in which levels of sophistication of various coarse models can be defined, an adaptive modeling strategy can be implemented to control modeling error. In the present work, the class of models is within those embodied in nonlinear continuum mechanics.

Keywords: mathematical model, modeling error, continuum mechanics, model adaptivity

Acknowledgments

We would like to thank Bob Chambers and Sam Key for reviewing this document. Bob Chambers, Sam Key, and Doug Adolf are also thanked for the many technical discussions pertaining to this research.

Contents

List of Figures

List of Tables

1 Introduction

Computational Engineering and Science (CES) is concerned with the use of mathematical and computational models to simulate physical events and engineering systems. In recent decades, the remarkable predictive power of computer models has led to advances in virtually every area of science and technology. Still, the most basic and fundamental step in developing a computer simulation of natural events is the selection of the model itself, a step left largely to heuristic arguments, judgment of the analyst, or based on incomplete empirical data. This most important step in computer simulation, if not done correctly, can be, and generally is, the source of the largest error.

In recognition of this fact, "code validation" (defined tersely by Roache [13, p.13] as "solving the right equations"), has become a major issue in CES. According to Roache, "Ultimately, code validation will come down to comparison (directly or indirectly) of code predictions with physical experiments." While we certainly agree with this pronouncement, we offer a supplementary approach to raw experimental validation that we refer to as *hierarchical modeling*, by which we mean the selection of various models from a large class of mathematical models of varying complexity and sophistication. The issue of validation, then, is first set in a mathematical framework in which modeling error can be defined with some precision, it being understood that various properties of the datum with respect to which such models are assessed must, itself, ultimately be compared with physical experiments.

The notion of hierarchical modeling and modeling error estimation was first advanced in connection with errors due to homogenization of heterogeneous materials [8, 9, 11, 12, 14] and of errors inherent in dimensional reduction to produce plate and shell models of three-dimensional bodies [10, 5, 6]. In these works, the notion of model adaptivity is introduced, in which modeling error estimates are used to adaptively select models capable of producing acceptable simulations (compared to a datum model).

In the present report, we present a general theory of error estimation and adaptivity within the broad framework of nonlinear continuum mechanics. We derive global error bounds for models of general classes of materials, and we present an algorithm for

model adaptivity. Finally, we consider a special case that can be analyzed in more detail.

2 Preliminaries: Problem Setting and Notation

2.1 Fine and Coarse Models

Our general goal is to estimate and control error due to the choice of a mathematical model within a class of possible models of certain physical phenomena. The modeling error is measured relative to what we shall call the *fine model*, which itself is also a mathematical model, but generally one of such detail, sophistication, and complexity, that all phenomena of interest are confidently captured, predicted, and simulated by it with adequate accuracy. All other models within the class of models are *coarser* or *simplified models*. The fine model, in general, may be intractable; while general and inclusive, it is often too complex to be used to obtain quantitative results. The "solution" of the fine model is, thus, never actually computed (except for possibly very special cases). The fine model is used only for a datum with respect to which modeling error in coarser models is measured. The fine model, for example, may characterize phenomena occurring at many spatial and temporal scales, and may include many interacting physical effects, while the coarser model may be characterized by averaged mechanical properties and simplified physical laws. Ultimately, the suitability of the fine model itself must be estimated by determining its predictive limits within the context of still larger classes of models or, more specifically, through physical experiments.

In this investigation, the fine model is provided by the nonlinear theory of continuous media: the fundamental laws and equations of nonlinear continuum mechanics.

2.2 Problem Setting: The Fine Model

We begin the characterization of the fine model by considering a material body in motion and under the action of prescribed external forces. We adopt a material ("Lagrangian") description of the motion in which the material particles (points) of the body in a fixed reference configuration are identified with positions $\boldsymbol{X}$ of points in

the closure of an open bounded region $\Omega_0 \subset \mathbb{R}^N$, $N = 1, 2$, or 3. The motion is characterized by the function

$$\boldsymbol{\chi}\colon \overline{\Omega}_0 \times \mathbb{R}^+ \to \mathbb{R}^N, \qquad \Omega_t = \boldsymbol{\chi}(\overline{\Omega}_0, t)$$

with $\boldsymbol{x} = \boldsymbol{\chi}(\boldsymbol{X}, t)$ the place of material particle $\boldsymbol{X}$ at time t. The displacement of $\boldsymbol{X}$ at time t is the vector

$$\boldsymbol{u}(\boldsymbol{X}, t) = \boldsymbol{\chi}(\boldsymbol{X}, t) - \boldsymbol{X}, \qquad \boldsymbol{X} \in \Omega_0.$$

In classical continuum mechanics, the motion (and deformation) of the body is governed by the linear and angular momentum equations,

$$\left.\begin{aligned} \rho_0(\boldsymbol{X})\,\frac{\partial^2 \boldsymbol{u}}{\partial t^2}(\boldsymbol{X}, t) - \mathrm{Div}\,(\boldsymbol{F}(\boldsymbol{u}; \boldsymbol{X}, t)\boldsymbol{P}(\boldsymbol{X}, t)) = \rho_0(\boldsymbol{X})\boldsymbol{b}(\boldsymbol{X}, t) \\ \boldsymbol{P}(\boldsymbol{X}, t) = \boldsymbol{P}(\boldsymbol{X}, t)^T \end{aligned}\right\} \tag{2.1}$$

for $\boldsymbol{X} \in \Omega_0$, $t > 0$, where Div is the divergence operator in the reference configuration and

ρ_0 = the mass density in the reference configuration

$\boldsymbol{F} = \boldsymbol{\nabla}\boldsymbol{\chi} = \boldsymbol{I} + \boldsymbol{\nabla}\boldsymbol{u} =$ the deformation gradient ($\boldsymbol{I}$ being the unit tensor)

$\boldsymbol{P}$ = the second Piola-Kirchhoff stress tensor

$\boldsymbol{b}$ = the body force per unit mass in the reference configuration

The displacement field (equivalently, the motion) satisfies the boundary conditions,

$$\left.\begin{aligned} \boldsymbol{u}(\boldsymbol{X}, t) = \overline{\boldsymbol{u}}(\boldsymbol{X}, t), \qquad \boldsymbol{X} \in \Gamma_D^0 \subset \partial\Omega_0,\ t \geq 0 \\ \boldsymbol{F}(\boldsymbol{u}; \boldsymbol{X}, t)\boldsymbol{P}(\boldsymbol{X}, t) \cdot \boldsymbol{n}_0(\boldsymbol{X}) = \boldsymbol{g}(\boldsymbol{X}, t), \qquad \boldsymbol{X} \in \Gamma_N^0 \subset \partial\Omega_0,\ t \geq 0 \end{aligned}\right\} \tag{2.2}$$

where $\overline{\boldsymbol{u}}$ is a prescribed displacement on a portion Γ_D^0 of the boundary $\partial\Omega_0$ and $\boldsymbol{g}$ is a prescribed surface traction per unit area in the reference configuration on a portion Γ_N^0 of $\partial\Omega_0$, $\partial\Omega_0 = \overline{\Gamma_D^0 \cup \Gamma_N^0}$. At $t = 0$, $\boldsymbol{u}$ also satisfies initial conditions,

$$\boldsymbol{u}(\boldsymbol{X}, 0) = \boldsymbol{U}_0(\boldsymbol{X}), \qquad \frac{\partial \boldsymbol{u}}{\partial t}(\boldsymbol{X}, 0) = \boldsymbol{V}_0(\boldsymbol{X}) \tag{2.3}$$

$\boldsymbol{U}_0$ and $\boldsymbol{V}_0$ being prescribed initial displacements and velocities, respectively.

Equations (2.1)-(2.2) define a classical model of the behavior of continuous media without regard to regularity of the data, the constitutive equations for stress or other

physical quantities, and without thermodynamic considerations. To put the fine model in a more general and useful setting, we shall now introduce a weak or variational form of the model.

2.3 Functional Setting

Let us introduce the space $V\ (= V(\Omega_0))$ of kinematically admissible displacements with domain Ω_0. Typically, we can take

$$V = \left\{ \boldsymbol{v} \in \left(H^1(\Omega_0)\right)^N ; \quad \gamma_0 \boldsymbol{v} = \boldsymbol{0} \text{ on } \Gamma_D^0 \right\} \tag{2.4}$$

where γ_0 is the trace operator. In many cases, depending on the structure and definition of $\boldsymbol{P}$, more general spaces may be identified for V (e.g. $\left(H^1(\Omega)\right)^N$ may be replaced by $\left(W^{1,p}(\Omega)\right)^N,\ p \neq 2$).

The Piola-Kirchhoff stress $\boldsymbol{P}$ is assumed to be determined by histories of the gradient of the motion (displacement), the temperature θ, and other internal variables, entropy, etc.), by constitutive equations of the form

$$\boldsymbol{P} = \boldsymbol{\mathcal{P}} \left(\boldsymbol{\nabla u}^t(s),\ \boldsymbol{A}^t(s) \right)$$

where we suppress the dependence on $\boldsymbol{X}$ and t for simplicity, and where

$$\begin{aligned} \boldsymbol{\nabla u}^t(s) &= \text{the displacement gradient history} \\ &= \{ \boldsymbol{\nabla u}(\cdot, t-s), \quad \boldsymbol{u}(\cdot,\ t-s) \in V, \quad t \geq s \geq 0 \} \end{aligned}$$

and $\boldsymbol{A}^t(s)$ denotes the histories of other constitutive variables. Hereafter, we shall suppress the histories $\boldsymbol{A}^t(s)$ and write, for simplicity, $\boldsymbol{P} = \boldsymbol{\mathcal{P}}(\boldsymbol{\nabla u}^t(s), t)$.

Summing up, a weak or variational form of the momentum equation is embodied

in the initial-value problem:

Given $\left(\Omega_0, \Gamma_D^0, \Gamma_N^0, \rho_0, \boldsymbol{b}, \boldsymbol{g}, \boldsymbol{U}_0, \boldsymbol{V}_0\right)$*, find, for each* $t \geq 0$*, the displacement field* $\boldsymbol{u}(\cdot, t) \in V + \{\overline{\boldsymbol{U}}\}$ *and the stress* $\boldsymbol{P} = \boldsymbol{\mathcal{P}}(\boldsymbol{\nabla} \boldsymbol{u}^t(s), t)$ *such that*

$$\int_{\Omega_0} \rho_0 \; \ddot{\boldsymbol{u}}(t) \cdot \boldsymbol{v} \; dX + \int_{\Omega_0} \boldsymbol{F}(\boldsymbol{u}; t) \boldsymbol{\mathcal{P}}\left(\boldsymbol{\nabla} \boldsymbol{u}^t(s), t\right) : \boldsymbol{\nabla} \boldsymbol{v} \; dX = \mathcal{F}(\boldsymbol{u}(t);\; \boldsymbol{v}, t) \quad \forall\, \boldsymbol{v} \in V,\; t > 0 \tag{2.5}$$

wherein $\boldsymbol{u}$, $\dot{\boldsymbol{u}}$ *satisfy (2.3) and* $\overline{\boldsymbol{u}} \in V$ *is such that* $\gamma_0 \overline{\boldsymbol{U}} = \overline{\boldsymbol{u}}$ *on* Γ_D^0.

Here $\ddot{\boldsymbol{u}} = \partial^2 \boldsymbol{u} / \partial t^2$, $\dot{\boldsymbol{u}} = \partial \boldsymbol{u} / \partial t$, $dX = dX_1 dX_2 dX_3$, and the dependence of the various integrand functions on $\boldsymbol{X}$ is understood.

The functional on the right side of (2.5) is the loading functional,

$$\mathcal{F}(\boldsymbol{u}(t);\; \boldsymbol{v}, t) = \int_{\Omega_0} \rho_0 \, \boldsymbol{b}(t) \cdot \boldsymbol{v} \, dX + \int_{\Gamma_N^0} \boldsymbol{g}(t) \cdot \boldsymbol{v} \, dS_0 \tag{2.6}$$

dS_0 being an element of surface area on $\Gamma_N^0 \subset \partial \Omega_0$. We note that, in terms of the tractions $\widetilde{\boldsymbol{g}}$ per unit surface area in the current configuration $\boldsymbol{\chi}\left(\Gamma_N^0\right) = \Gamma_N$,

$$\boldsymbol{g}(\boldsymbol{X}, t) = \det \boldsymbol{F}(\boldsymbol{u}; t) \times \left| \boldsymbol{F}(\boldsymbol{u}; t)^{-T} \, \boldsymbol{n}_0(\boldsymbol{X}) \right| \widetilde{\boldsymbol{g}}\left(\boldsymbol{\chi}(\boldsymbol{X}, t), t\right). \tag{2.7}$$

For example, if $\widetilde{\boldsymbol{g}}$ is a pressure load of intensity $-\pi$ on Γ_N, (see, e.g., Ciarlet [7]),

$$\boldsymbol{g}(\boldsymbol{X}, t) = -\pi \det \boldsymbol{F}(\boldsymbol{u}; t) \, \boldsymbol{F}(\boldsymbol{u}; t)^{-T} \, \boldsymbol{n}_0(\boldsymbol{X}).$$

Thus $\mathcal{F}(\boldsymbol{u}(t);\; \boldsymbol{v}, t)$ may be a highly nonlinear function of $\boldsymbol{u}(t)$ (precisely, $\boldsymbol{\nabla} \boldsymbol{u}(t)$); hence the notation used on the left of (2.6).

2.4 The Coarse Model

We now consider the motion of a material body occupying the same reference configuration Ω_0 at $t = 0$ as that appearing in the fine model and subjected to the same external forces $(\boldsymbol{b}, \boldsymbol{g})$, boundary conditions, and initial conditions, but whose mechanical response is characterized by a "simplified" collection of constitutive equations.

The displacement field in this case is denoted $\boldsymbol{u}_0$. Instead of (2.5), the weak form of the linear momentum equation for the coarse model is

$$\int_{\Omega_0} \rho_0 \, \ddot{\boldsymbol{u}}_0(t) \cdot \boldsymbol{v} \, dX + \int_{\Omega_0} \boldsymbol{F}(\boldsymbol{u}_0; t) \boldsymbol{\mathcal{P}}_0 \left(\boldsymbol{\nabla} \boldsymbol{u}_0^t(s), t \right) : \boldsymbol{\nabla} \boldsymbol{v} \, dX = \mathcal{F}(\boldsymbol{u}_0; \boldsymbol{v}, t)$$
$$\forall \, \boldsymbol{v} \in V, \ t > 0 \quad (2.8)$$

where $\boldsymbol{u}_0(\cdot, t) \in V + \{\overline{\boldsymbol{U}}\}$ and $\boldsymbol{P} = \boldsymbol{\mathcal{P}}_0 \left(\boldsymbol{\nabla} \boldsymbol{u}_0^t(s), t \right)$ *satisfy the same boundary and initial conditions as* $\boldsymbol{u}$ *and* $\boldsymbol{P}$ *in* (2.5).

It may also be possible that the density ρ for the coarse model differs from that of the fine model. We address this possibility later.

3 A Global Estimate of Modeling Error

3.1 Residual Modeling Error

Let us assume that the motion (particularly, the displacement field) $\boldsymbol{u}_0(t) \in V$ of the coarse model is known for all $t \in [0, T]$. Then the modeling error at time t is defined by the functions

$$\left.\begin{aligned} \boldsymbol{e}_{\boldsymbol{u}}(t) &= \boldsymbol{u}(t) - \boldsymbol{u}_0(t) \\ \boldsymbol{E}_{\boldsymbol{P}}(t) &= \boldsymbol{\mathcal{P}} \left(\boldsymbol{\nabla} \boldsymbol{u}^t(s), t \right) - \boldsymbol{\mathcal{P}} \left(\boldsymbol{\nabla} \boldsymbol{u}_0^t(s), t \right) \\ e_{\mathcal{F}}(\boldsymbol{v}, t) &= \mathcal{F}(\boldsymbol{u}(t); \boldsymbol{v}, t) - \mathcal{F}(\boldsymbol{u}_0(t); \boldsymbol{v}, t) \end{aligned}\right\} \quad (3.1)$$

Introducing (3.1) into (2.5) (by eliminating $\boldsymbol{u}(t)$, $\boldsymbol{\mathcal{P}}(\boldsymbol{u}^t(s), t)$ and $\mathcal{F}(\boldsymbol{u}(t); \boldsymbol{v}, t)$), we arrive at the equation

$$\begin{aligned} \int_{\Omega_0} \rho_0 \ddot{\boldsymbol{e}}_{\boldsymbol{u}}(t) \cdot \boldsymbol{v} \ dX + \int_{\Omega_0} \boldsymbol{\nabla} \boldsymbol{e}_{\boldsymbol{u}}(t) \boldsymbol{\mathcal{P}}(\boldsymbol{\nabla} \boldsymbol{u}_0^t(s), t) \colon \boldsymbol{\nabla} \boldsymbol{v} \ dX \\ + \int_{\Omega_0} \boldsymbol{F}(\boldsymbol{u}_0 + \boldsymbol{e}_{\boldsymbol{u}}; t) \boldsymbol{E}_{\boldsymbol{P}}(t) \colon \boldsymbol{\nabla} \boldsymbol{v} \ dX \\ - \boldsymbol{e}_{\mathcal{F}}(\boldsymbol{v}, t) = \mathcal{R}(\boldsymbol{u}_0^t(s); \boldsymbol{v}, t), \qquad \forall \boldsymbol{v} \in V, \ t > 0 \end{aligned} \quad (3.2)$$

where the functional $\mathcal{R}(\cdot; \boldsymbol{v}, t)$ is the *global modeling residual*,

$$\mathcal{R}(\boldsymbol{u}_0^t(s); \boldsymbol{v}, t) = \int_{\Omega_0} \boldsymbol{F}(\boldsymbol{u}_0; t) \ \Delta \boldsymbol{\mathcal{P}} \left(\boldsymbol{\nabla} \boldsymbol{u}_0^t(s), t \right) : \boldsymbol{\nabla} \boldsymbol{v} \, dX \quad (3.3)$$

with $\Delta\boldsymbol{\mathcal{P}}$ the stress error,

$$\Delta\boldsymbol{\mathcal{P}}\left(\boldsymbol{\nabla u}_0^t(s),t\right) := \boldsymbol{\mathcal{P}}_0\left(\boldsymbol{\nabla u}_0^t(s),t\right) - \boldsymbol{\mathcal{P}}\left(\boldsymbol{\nabla u}_0^t(s),t\right). \tag{3.4}$$

Thus, once the coarse model is used to obtain $\boldsymbol{u}_0(t)$ for all $t \in [0,T]$ of interest, the residual functional $\mathcal{R}(\cdot\,;\boldsymbol{v},t)$ is determined from known data (modulo other mechanical and thermodynamical effects characterized by other constitutive equations, constraints, and the balance of energy equations.)

Next, let $\mathcal{E}$ denote the linear functional on V, defined by the nonlinear evolutions of error components on the left side of (3.2):

$$\begin{aligned}\mathcal{E}(\boldsymbol{v},t) := &\int_{\Omega_0} \rho_0 \ddot{\boldsymbol{e}}_{\boldsymbol{u}}(t)\cdot\boldsymbol{v}\; dX + \int_{\Omega_0} \boldsymbol{\nabla e}_{\boldsymbol{u}}(t)\boldsymbol{\mathcal{P}}(\boldsymbol{\nabla u}_0^t(s),t)\colon \boldsymbol{\nabla v}\; dX \\ &+ \int_{\Omega_0} \boldsymbol{F}(\boldsymbol{u}_0+\boldsymbol{e}_{\boldsymbol{u}};t)\boldsymbol{E}_{\boldsymbol{P}}(t)\colon \boldsymbol{\nabla v}\; dX - e_{\mathcal{F}}(\boldsymbol{v},t), \\ &\qquad\qquad \forall \boldsymbol{v}\in V,\ t>0. \end{aligned} \tag{3.5}$$

With these notations, (3.2) can be rewritten compactly as

$$\boxed{\mathcal{E}(\boldsymbol{v},t) = \mathcal{R}\left(\boldsymbol{u}_0^t(s);\boldsymbol{v},t\right), \qquad \forall\,\boldsymbol{v}\in V,\ t>0}\,. \tag{3.6}$$

From (3.3) and Schwarz's inequality,

$$\mathcal{R}\left(\boldsymbol{u}_0^t(s);\ \boldsymbol{v},t\right) \le \zeta(t)\|\boldsymbol{v}\|_{1,\Omega_0} \tag{3.7}$$

where $\zeta(t)$ is the global, *a posteriori*, modeling error indicator,

$$\zeta(t) = \left\{\int_{\Omega_0} \left|\boldsymbol{F}(\boldsymbol{u}_0(t);t)\ \Delta\boldsymbol{\mathcal{P}}(\boldsymbol{\nabla u}_0^t(s),t)\right|^2 dX\right\}^{1/2} \tag{3.8}$$

and

$$\|\boldsymbol{v}\|_{1,\Omega_0} = \left\{\int_{\Omega_0} (\boldsymbol{v}\cdot\boldsymbol{v} + \boldsymbol{\nabla v}:\boldsymbol{\nabla v})\, dX\right\}^{1/2}. \tag{3.9}$$

Introducing (3.7) into (3.6), dividing by $\|\boldsymbol{v}\|_{1,\Omega_0}$, and taking the supremum of the result over all V, we have the *global error bound*:

$$\boxed{\|\mathcal{E}(t)\|_{V'} \le \zeta(t)}\,. \tag{3.10}$$

Here $\|\cdot\|_{V'}$ denotes the norm of the dual space V' of V.

3.2 Remarks and Extensions

Several remarks are in order concerning the error bound (3.10) and the steps leading to it.

3.2.1 The Space V

The spaces of admissible displacement for the fine and coarse models may differ. Thus, (2.8) may be valid for all $\boldsymbol{v}$ in a smaller space V_0, the ensuing error analysis remains valid whenever $V_0 \subset V$.

3.2.2 Fine Model Density

The mass density ρ of the fine and coarse models may differ. For example, the fine model may involve characterizations of heterogeneous material with $\rho_0 = \rho_0(\boldsymbol{X})$ varying rapidly over Ω_0, while the coarse model may involve the use of effective properties of materials with ρ_0 a constant.

Let ρ_{00} denote the mass density field in the coarse model. The first term on the left of (2.8) becomes $\int_{\Omega_0} \rho_{00}\, \ddot{\boldsymbol{u}}_0 \cdot \boldsymbol{v}\, dX$ and, instead of (3.6), we have, for $\boldsymbol{v} \in V$,

$$\widehat{\mathcal{E}}(\boldsymbol{v}, t) = \mathcal{E}(\boldsymbol{v}, t) - \int_{\Omega_0} e_\rho \ddot{\boldsymbol{u}}_0(t) \cdot \boldsymbol{v}\, dX \tag{3.11}$$

where

$$e_\rho = \rho_0 - \rho_{00}. \tag{3.12}$$

The remainder of the analysis is the same with $\mathcal{E}$ replaced by $\widehat{\mathcal{E}}$.

3.2.3 The Error Measure $\mathcal{E}$

It is not necessary to calculate the quantity $\|\mathcal{E}\|_{V'}$. Inequality (3.10) merely indicates what measure of error is bounded by the residual indicator ζ at time t. Nevertheless, an interpretation of this error can be given by introducing the $\boldsymbol{H}^1$-inner product,

$$(\boldsymbol{u}, \boldsymbol{v})_{1,\Omega_0} := \int_{\Omega_0} (\boldsymbol{\nabla u} : \boldsymbol{\nabla v} + \boldsymbol{u} \cdot \boldsymbol{v}) dX, \qquad \boldsymbol{u}, \boldsymbol{v} \in V. \tag{3.13}$$

Next, let $\boldsymbol{G}(t)$ be the solution of the boundary-value problem,

$$(\boldsymbol{G}(t), \boldsymbol{v})_{1,\Omega_0} = \mathcal{E}(\boldsymbol{v}, t), \qquad \forall\, \boldsymbol{v} \in V. \tag{3.14}$$

Then

$$\|\boldsymbol{G}(t)\|_{1,\Omega_0} = \|\mathcal{E}(t)\|_{V'} \leq \zeta(t). \tag{3.15}$$

The error measure $\boldsymbol{G}(t)$ can thus be thought of as an H^{-1}-projection of the various error functionals defined by $\mathcal{E}$. Indeed, if $\langle\cdot,\cdot\rangle$ denotes duality paring on $V' \times V$, and $\boldsymbol{v} = \boldsymbol{\varphi} \in \boldsymbol{\mathcal{D}}(\Omega_0)$,

$$\langle(-\boldsymbol{\Delta} + \boldsymbol{I})\boldsymbol{G}(t) - \mathcal{E}(t), \boldsymbol{\varphi}\rangle = 0, \qquad \forall\, \boldsymbol{\varphi} \in \boldsymbol{\mathcal{D}}(\Omega_0) \tag{3.16}$$

where $\boldsymbol{\Delta}$ is the vector-Laplacian. Then $\boldsymbol{G}(t)$ represents the global smoothing, $\boldsymbol{G}(t) = (-\boldsymbol{\Delta} + \boldsymbol{I})^{-1}\mathcal{E}(t)$.

3.2.4 Other Modeling Errors

The bound (3.10) is obtained by comparing only models of the linear momentum equation; (angular momentum is presumed to be conserved in both fine and coarse models). Other physical processes may be part of the fine and coarse models which are not adequately captured by this analysis. For a more complete picture, thermodynamic models must be included, and we must augment the momentum equation with the energy equations and possibly with other constraints not shared by the coarse model. We shall take up these issues in a later work.

4 Model Adaptivity Based on Global Bounds

Let us suppose that the domain Ω_0 is partitioned into a collection of non-overlapping subdomains Ω_{0K}:

$$\mathcal{P}\colon\ \overline{\Omega}_0 = \bigcup_{K=1}^{N(\mathcal{P})} \overline{\Omega}_{0K}; \qquad \Omega_{0K} \cap \Omega_{0J} = \varnothing,\ K \neq J. \tag{4.17}$$

The global model error indicator $\zeta(t)$ of (3.8) can be written as the sum,

$$\zeta(t) = \left\{ \sum_{K=1}^{N(\mathcal{P})} \zeta_K^2(t) \right\}^{1/2} \tag{4.18}$$

where

$$\zeta_K^2(t) = \int_{\Omega_{0K}} \left| \boldsymbol{F}(\boldsymbol{u}_0(t); t)\ \Delta\boldsymbol{\mathcal{P}}\left(\boldsymbol{\nabla}\boldsymbol{u}_0^t(s), t\right)\right|^2 dX \tag{4.19}$$

with $\Delta\boldsymbol{\mathcal{P}}$ defined by (3.4).

The $\zeta_K(t)$ are thus the contributions of the error over Ω_{0K} to the global modeling error $\zeta(t)$. They do not represent local modeling errors, as the actual local error is generally polluted by errors in remote subdomains. Nevertheless, the $\zeta_K(t)$ are used as an indication of the relative error in various subdomains and to identify subdomains where the error in the predictions of the coarse model may be large. For example, if

$$\zeta_K(t) < \alpha \max_{K \in \mathcal{P}} \zeta_K,$$

where $\alpha \in (0, 1)$ is a preselected parameter, we may declare the coarse model acceptable for subdomain Ω_{0K}; otherwise, the modeling error must be reduced by adding more sophistication to the coarse model. Exactly how this can be done will vary depending on characteristics of the fine model and, since the fine model is often intractable, the process can fail if an error tolerance cannot be met by any coarser model in the class.

5 Application to Nonlinear Viscoelastic Polymers

An application of the present theory to a family of material laws for polymers is now considered. First, a brief overview of the nonlinear viscoelastic family will be given and followed by a discussion of how material model adaptivity is currently implemented for this model. Both non-adaptive and adaptive results using the various models in this material class will be given. Further details and equations describing the fine model and its associated coarse model approximations are given in the Appendix.

5.1 Nonlinear Viscoelasticity (NLVE) Overview

The constitutive law developed by Chambers, Adolf and Caruthers [4] describes the nonlinear viscoelastic response of glassy polymers. This material model was developed using a thermodynamically consistent rational mechanics approach. The material constants in the model were fit to an epoxy so that a wide range of physical phenomena can be modeled both comprehensively and quantitatively. A key feature of the detailed nonlinear viscoelastic model used in this example is that the physical phenomena of interest, such as yielding, volume recovery, or enthalpy relaxation, are captured through

Table 5.1: Models in the NLVE family ordered in terms of computational expense.

Model	Material Relaxations
(1B) Rubbery elastic	all relaxations completed by end of time step
(1D) Pseudo elastic	no relaxations over time step
(2B) WLF	$a = a(\theta)$
(3B) Configurational entropy	$a = a(\theta$, volumetric strain)
(4B) Configurational energy	$a = a(\theta$, volumetric strain, stress)

the use of a material clock assuming rheological simplicity. The material/reduced time scale on which viscoelastic relaxations proceed is controlled by the horizontal shift factor a as given by Eq. (A.6) in the Appendix.

The various models in the NLVE family are delineated based on what physics are incorporated into $\log_{10}[a]$. The fine scale model includes the effects of thermal, volumetric strain and stress histories in the horizontal shift factor which is given in terms of the configurational energy. The first level of approximation has a shift factor which depends upon configurational entropy and includes the effects of the temperature and volume histories on $\log_{10}[a]$. A still coarser model is where $\log_{10}[a]$ depends only on the current temperature through the well-known WLF equation. This model assumes thermodynamic equilibrium and has been found to be valid for polymers under moderate stresses at temperatures ranging from the glass transition temperature θ_g to $\theta_g + 100\,\mathrm{K}$. For polymers under moderate stresses at temperatures below θ_g, the configurational entropy model must be used. Finally, two elastic levels are defined which correspond to no material relaxations occurring over the current time step (pseudo elastic model) or all of the relaxations reaching completion by end of the current time step (rubbery elastic model). A summary of the NLVE models is presented in Table 5.1 where they have been numbered and ordered according to increasing computational cost.

5.2 NLVE Adaptivity

Using the conceptual idea presented in Section 4, local error measures will be used to select from among the material models in the NLVE family, even though only a

global error bound was formally derived. The material model adaptivity in the present work is an explicit scheme performed on an element by element basis at the end of each time step as needed. That is, the model to be used for each element in the next time step is selected based upon the error measures for the time step which has just been converged. The computations pertaining to adaptive modeling can be best understood by considering the computations necessary for a single time step. For instance, consider the solution up to time $t - \Delta t$ to have been computed using an adaptive solution, in which the models used can vary both in space and time with a single model used for each element over each time step. Two types of calculations are then performed for the current time step which ends at time t. One is to compute the deformed state at t and the other is to compare how the stresses at t would differ using various models so that adaptivity can be performed.

The first set of calculations involves iteratively finding the displacements and state variable histories corresponding to equilibrium. During these calculations, a single model of the family is used for each element. The second set of calculations are designed to obtain the *a posteriori* error indicators that are used to select the material model for the next time step. These estimates represent the differences in the stresses computed using two models, which arise from the differences in the state variables, as the Hencky stress tensor is the same in each model. These state variables are updated using their previously computed values at $t-\Delta t$ along with the displacements computed for equilibrium at t. The state variable updates for each model involve different approximations of the elapsed time on the material time scale/clock (i.e., how fast the viscoelastic relaxations are proceeding over the current time step). For this reason, the error estimates are local in time, i.e., they characterize the error over the current time step. The accumulation of errors from previous time steps are not considered.

For the adaptive NLVE results presented in this report, the adaptive solution is based upon a slightly different error indicator than that presented previously in this report. The adaptive error indicator $\bar{\zeta}$ between two different models is calculated and reported as a percentage in fractional form (e.g., 10% error is reported as 0.1). The

error indicator $\bar{\zeta}$ at time t is defined as follows:

$$\bar{\zeta}_t^2(t) = \left|\boldsymbol{F}(\boldsymbol{u}_E(t);t)\left[\boldsymbol{\mathcal{P}}_N\left(\boldsymbol{\nabla}u_E^t(s),\boldsymbol{A}_{E,N}^t(s);\,t\right)\right.\right. \tag{5.1}$$

$$\left.\left.-\boldsymbol{\mathcal{P}}_M\left(\boldsymbol{\nabla}u_E^t(s),\boldsymbol{A}_{E,M}^t(s);\,t\right)\right]\right|^2 \tag{5.2}$$

$$\bar{\zeta}_b^2(t) = \left|\boldsymbol{F}(\boldsymbol{u}_E(t);t)\left[\boldsymbol{\mathcal{P}}_N\left(\boldsymbol{\nabla}u_E^t(s),\boldsymbol{A}_{E,N}^t(s);\,t\right)\right]\right|^2 \tag{5.3}$$

$$\bar{\zeta}(t) = \sqrt{\bar{\zeta}_t^2(t)/\bar{\zeta}_b^2(t)} \tag{5.4}$$

where the stress dependence on the state variable history has been written explicitly. Here, the subscript E refers to the model(s) used for equilibrium throughout the deformation history and the N and M subscripts, respectively, denote the model used from $t-\Delta t$ to t in finding the converged equilibrium state at t and the model to which the comparison is being made. Here, the state variable history $\boldsymbol{A}_{E,N}^t(s)$ is defined as follows:

$$\boldsymbol{A}_{E,N}^t(s) = \begin{cases} \boldsymbol{A}_E(t-s) & t \geq s \geq \Delta t \quad (0 \leq t-s \leq t-\Delta t) \\ \boldsymbol{A}_N(t-s) & \Delta t \geq s \geq 0 \quad (t-\Delta t \leq t-s \leq t) \end{cases} \tag{5.5}$$

The state variable history $\boldsymbol{A}_{E,M}^t(s)$ is defined similarly. The relative error $\bar{\zeta}$ is a local quantity calculated for each element at its centroid (i.e., $\bar{\zeta}_t$ and $\bar{\zeta}_b$ are calculated for the same element).

If a coarse model has been used, it is necessary to assess whether it has been accurate over the current time step. This assessment is made by comparing the coarse and fine models, where of course, the finest material description here is the configurational energy model (4B). Because none of the other models incorporate all of the physics contained in the configurational energy model (4B), anytime the constitutive law in a given element appears to be inaccurate (i.e., $\bar{\zeta}$ is larger than a user-prescribed tolerance), the configurational energy model (4B) is then selected in that element for the next time step.

For the case where the model used for equilibrium provides accurate results, either that model or perhaps a coarser model can be used over the next time step. The error estimate $\bar{\zeta}$ is calculated, this time by comparing the model used for equilibrium and a coarser model. Hence, a direct comparison between such a coarser model and the fine model is never made, unless of course, the fine model is used for equilibrium. For all

other cases, only an indirect comparison is made. The coarsest model which appears to be accurate ($\bar{\zeta}$ is small enough) is selected for calculations in the next time step.

5.3 Numerical Results

The present example considers a square plate with a centrally-located hole under tension. Symmetry boundary conditions are used on two edges of the plate so that only one-fourth of the plate has to be modeled. The plate has a length of 50.8 mm, a thickness of 0.635 mm and hole with a radius of 6.35 mm. The plate geometry is shown in Fig. 1. The plate is assumed to be stress free and in thermodynamic equilibrium in the initial state. The temperature field is uniform and held constant at θ_g throughout the entire analysis. The tension boundary conditions are applied as a prescribed displacement on the exterior edge that is perpendicular to the global X axis. The prescribed displacement in the X direction increases linearly with time at a rate of 0.254 mm/sec.

Two types of results are computed. In the first set of experiments, we assess the performance of the error estimates using the same model over the entire analysis. In the second set of experiments, we produce adaptive solutions prescribing three different error tolerances for the local error indicator $\bar{\zeta}$.

5.3.1 Single Model Results

The reference solution for this example is computed using the configurational energy model (4B), the most complete model with respect to material description, for all elements at all time steps in the JAS-3D [2] finite element code. A total of 867 elements are used to discretize one-fourth of the plate. The mesh is shown in Fig. 1 along with twenty regions into which the elements have been grouped. The solution is computed up to a time of 10 seconds using 100 uniform time steps. The spatial and time discretizations are assumed to be sufficient for convergence using any of the models in the NLVE family. That is, the approximation errors in the numerical solutions are ignored at present. The interaction between modeling errors and approximation errors will be explored in a later work.

Contours of the Cauchy stress component σ_{xx} for the reference solution are shown in Fig. 2. For these and all other contour plots presented for this example, the results

are presented on deflected meshes. Contours of σ_{yy} are not shown for brevity. For relatively small times, the nonlinear viscoelastic results give stress concentrations that resemble what would occur for a similar elastic case. That is, the location of the highest tensile σ_{xx} occurs at the intersection of the hole and symmetry plane perpendicular to the X-axis, whereas the highest compressive stress σ_{yy} occurs at the intersection of the hole and the symmetry plane perpendicular to the Y-axis. However, as the time and loading increase, the σ_{xx} stress concentration moves slightly along the X-symmetry plane away from the hole. These changes in the distribution of σ_{xx} result from the fact that the stresses affect the rate at which viscoelastic relaxations occur in the configurational energy model (4B). The compressive σ_{yy} stresses are not large enough to cause yielding at the intersection of the Y-symmetry plane and the hole. Hence, the location of the highest compressive σ_{yy} remains stationary.

The results for σ_{xx} for the case where the WLF model (2B) is used are shown as contour plots in Fig. 3. Because the shift factor of the WLF model (2B) depends only on the current temperature, which is chosen to be spatially uniform and constant for all time, the viscoelastic relaxations proceed at a uniform rate for all elements over all time steps. Hence, the stress concentration regions do not move as the time and loading increase for this linear viscoelastic model. The contribution of each element to the square of the global error indicator ζ^2 at several discrete times are shown in Fig. 4. Here, the global error indicator compares the WLF (2B) and configurational energy (4B) models. These contributions are ζ_K^2 as defined by Eq. (4.19) with each element taken as a separate subdomain. As expected, the most significant contributions to ζ^2 come from the area where the tensile stress concentration occurs, which is where the error in the stress is the largest. The region of relatively high ζ_K^2 increases around the top of the hole as time evolves. It should be kept in mind that here the contributions to ζ^2 at the end of a time step have the configurational energy model (4B) results estimated using the WLF (2B) displacement solution along with the WLF (2B) results for the state variable histories up to the start of the time step. Obviously, the accuracy of the stresses predicted for the configurational energy model (4B) is questionable for large times when no effort has been made at controlling the modeling errors. Also note that besides the difference in the stresses between the WLF (2B) and configurational energy (4B) models, the size of ζ_K^2 is, of course, affected by the size of the subdomain

K, i.e., the size of element K here.

Fig. 5 shows the results for σ_{xx} at several discrete times when the configurational entropy model (3B) is used. In addition, the evolution of the element-wise contributions to the global error indicator are computed and shown in Fig. 6. Although the configurational entropy model (3B) includes more physics than does the WLF model (2B), it still does not include stress effects in the material clock. Hence, similar to the WLF model (2B), the locations of the highest tensile and compressive stresses do not move as the loading and time increase. However, the stresses from the configurational entropy model (3B) are slightly more accurate than those from the WLF model (2B). Hence, although the element-wise contributions to ζ^2 show similar trends as those from the WLF model (2B), the values are somewhat smaller.

5.3.2 Adaptivity Results

Adaptive solutions based on the local error estimate $\bar{\zeta}$ given by Eq. (5.4) are now presented. Three different tolerances (0.05, 0.03, and 0.01) are used. In each case, the configurational energy model (4B) is chosen as the initial constitutive law in all elements. As the solution evolves, the models used are selected on an element by element, time step by time step basis.

We first show in Fig. 7 the time history of the percentage of elements using each model in the NLVE family for the three tolerances. We then show, in the case where the tolerance is set to 0.05, the Cauchy stress σ_{xx} and the element-wise distributions of the models used for the equilibrium calculations in Fig. 8 and Fig. 9 respectively. In the following figure, Fig. 10, we show σ_{xx} at 10.0 sec and the element-wise distributions of the models used over the time step ending at 10.0 sec for the tolerances 0.03 and 0.01.

The tolerance is set to 0.05. The trends in σ_{xx} (see Fig. 8) from this adaptive solution resemble the trends predicted in the configurational energy (4B) reference solution. However, the computed magnitudes of σ_{xx} from this adaptive solution appear to be somewhat larger than those from the reference solution. We observe in Fig. 7 that after one time step (i.e., the first 0.1 second), all elements switch from the configurational energy model (4B) to the WLF model (2B). At $t = 1.2$ sec, the configurational energy model (4B) begins to be used by some of the elements located

at the top of the hole where the highest tensile σ_{xx} appear. The configurational energy model (4B) usage then spreads out diagonally over the surrounding region. At $t = 3.8$ sec, the pseudo elastic model (1D) begins to be used by elements at the intersection of the $Y = 0$ plane and the side where the displacement boundary conditions are applied. The usage of the pseudo elastic model (1D) then spreads inward. There is some slight chattering in the model selection for individual elements. However, by approximately $t = 7$ sec, a distinct pattern has emerged for the model usage by the elements. For the elements where the stress is relatively high, the configurational energy model (4B) is used, whereas the pseudo elastic model (1D) is used for almost all other elements. For a tolerance level of 0.05, the rubbery elastic model (1B) is never accurate enough to be used. These trends in model usage appear to be reasonable.

The tolerance is set to 0.03. Although contours of σ_{xx} at other times are not shown in Fig. 10, the results for σ_{xx} do follow the same trends as those found in the configurational energy (4B) reference solution. The magnitudes of the stresses in this adaptive solution match those in the reference solution more closely than did those in the adaptive solution with the 0.05 tolerance. The evolution of the spatial distribution of the models used resembles to a certain extent that for the looser tolerance of 0.05. However, the configurational energy model (4B) is used over more elements with this tighter tolerance of 0.03. Once again, the rubbery elastic model (1B) is not accurate enough to be used at any stage in the time/load ranges considered in this example.

The tolerance is set to 0.01. Although not verifiable by the figures presented, the evolution of σ_{xx} in this adaptive solution very closely mimics that in the reference solution. Similar to the other two adaptive solutions, all elements switch to the WLF model (2B) after one time step. The usage of the configurational energy model (4B) is more prevalent in this solution as is evident from Figs. 7 and 10. Also evident is that most of the elements that do not use the configurational energy model (4B) over a given time step use the WLF model (2B). Recall that the WLF model (2B) accounts for viscoelastic relaxations with only temperature effects taken into account in the material clock. On the other hand, the pseudo elastic model (1D) does not allow any relaxations to occur over any of the time steps in which it is used. Hence, even though the WLF model (2B) does not capture the stress effects in $\log_{10}[a]$, it is still more accurate than the pseudo elastic model (1D). Thus as the adaptive tolerance

is tightened, the selection of the WLF model (2B) over the pseudo elastic model (1D) for elements away from the relatively high tensile stresses is as expected. Here, the error tolerance is tight enough that neither of the elastic models is ever used.

Some other stress results that may be useful include the history of the average stress over a group of elements or how the stress varies along a given spatial path at a given time. For brevity only a few of these types of results will be presented. The results for σ_{xx} versus distance along path A (see Fig. 1) are shown in Fig. 11 at several times for all three adaptive solutions along with the reference solution. The data points correspond to the centroids of the elements making up path A. We observe that all of the adaptive solutions exhibit the same trends as the reference solution with the accuracy increasing as the tolerance is tightened.

The history of the average stresses over regions 1 and 5 identified in Fig. 1 are shown in Fig. 12. The averaging scheme was based upon the initial volumes of the elements making up each region. Once again, all of the generated adaptive solutions exhibit the same trends as the reference solution, yet with a better accuracy as the tolerance is decreased.

6 Concluding Remarks

In the present report, we have discussed our preliminary work on modeling error and adaptivity within the framework of nonlinear continuum mechanics. Our theoretical result, namely a bound on the modeling error, has been applied to the special case of nonlinear viscoelasticity. The first set of numerical results appear to be very encouraging. Indeed, we have been able to produce adaptive solutions, using different models in various regions of the computational domain, almost as accurate as the solution obtained with the finest model. We are now convinced that this is a promising approach to modeling error and adaptivity. Nevertheless more numerical experiments are needed in order to better assess the performance of our algorithm for modeling adaptivity. Furthermore, thermodynamic and possibly other considerations must be taken into account so that a more robust adaptivity scheme can be developed for the nonlinear viscoelastic model studied here and other material models.

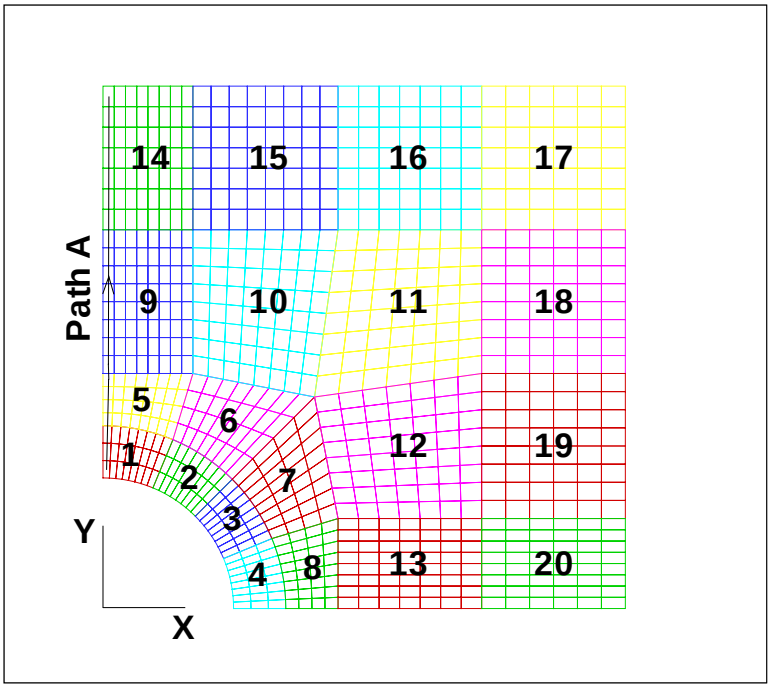

Figure 1: Quarter plate geometry and mesh. In addition, the elements have been grouped into twenty numbered regions for reporting average quantities over a region. Also shown is path A which connects the centroids of the elements on the vertical symmetry edge.

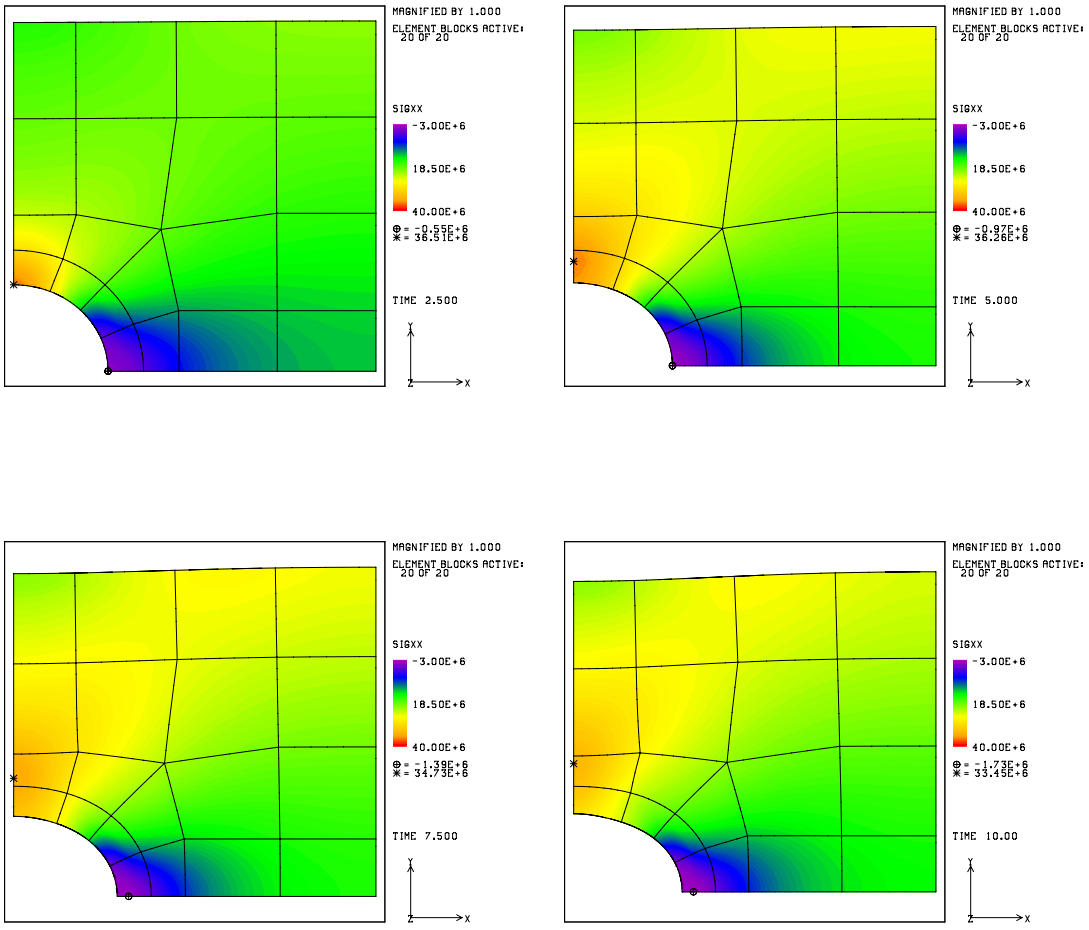

Figure 2: Reference solution: Cauchy stress σ_{xx} at $t = 2.5$, 5.0, 7.5 and 10 seconds (left to right, top to bottom) for the case where the configurational energy model (4B) is used for all calculations.

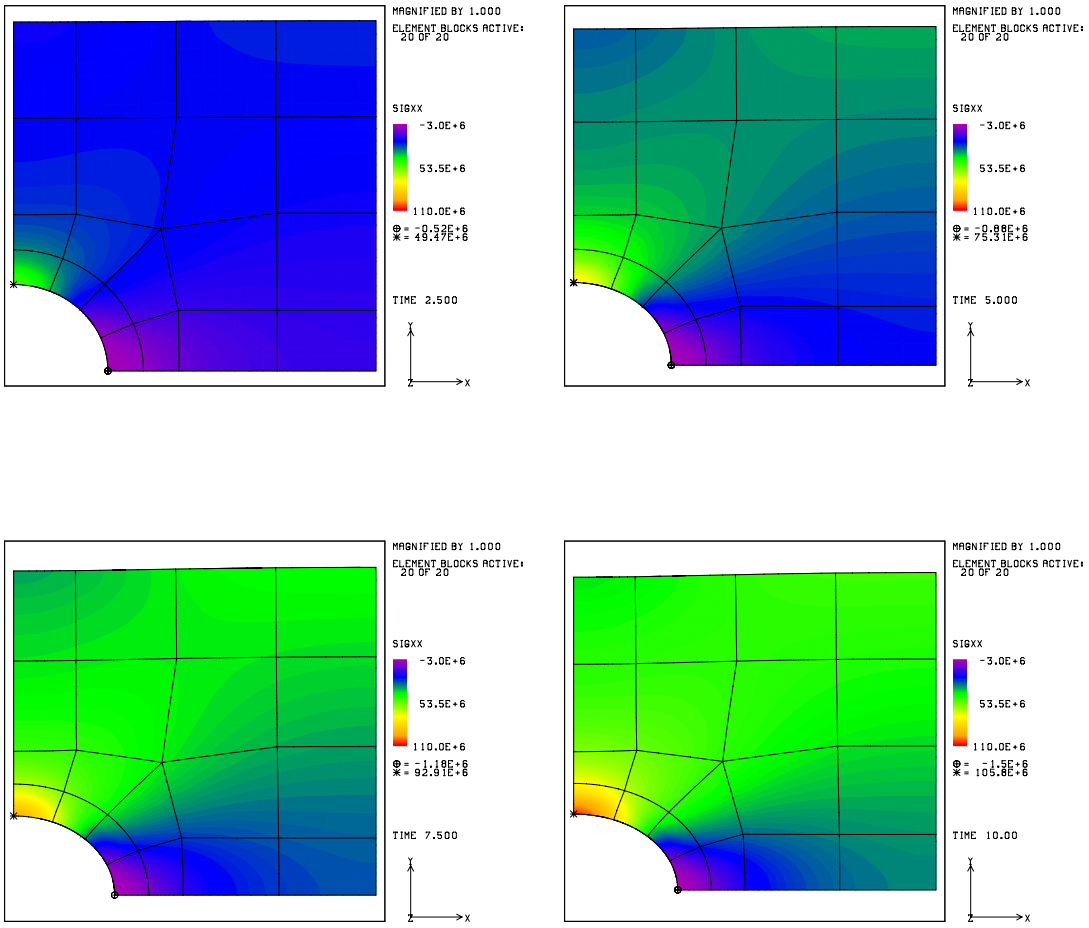

Figure 3: Cauchy stress σ_{xx} at $t = 2.5$, 5.0, 7.5 and 10 seconds (left to right, top to bottom) for the case where the WLF model (2B) is used for all calculations.

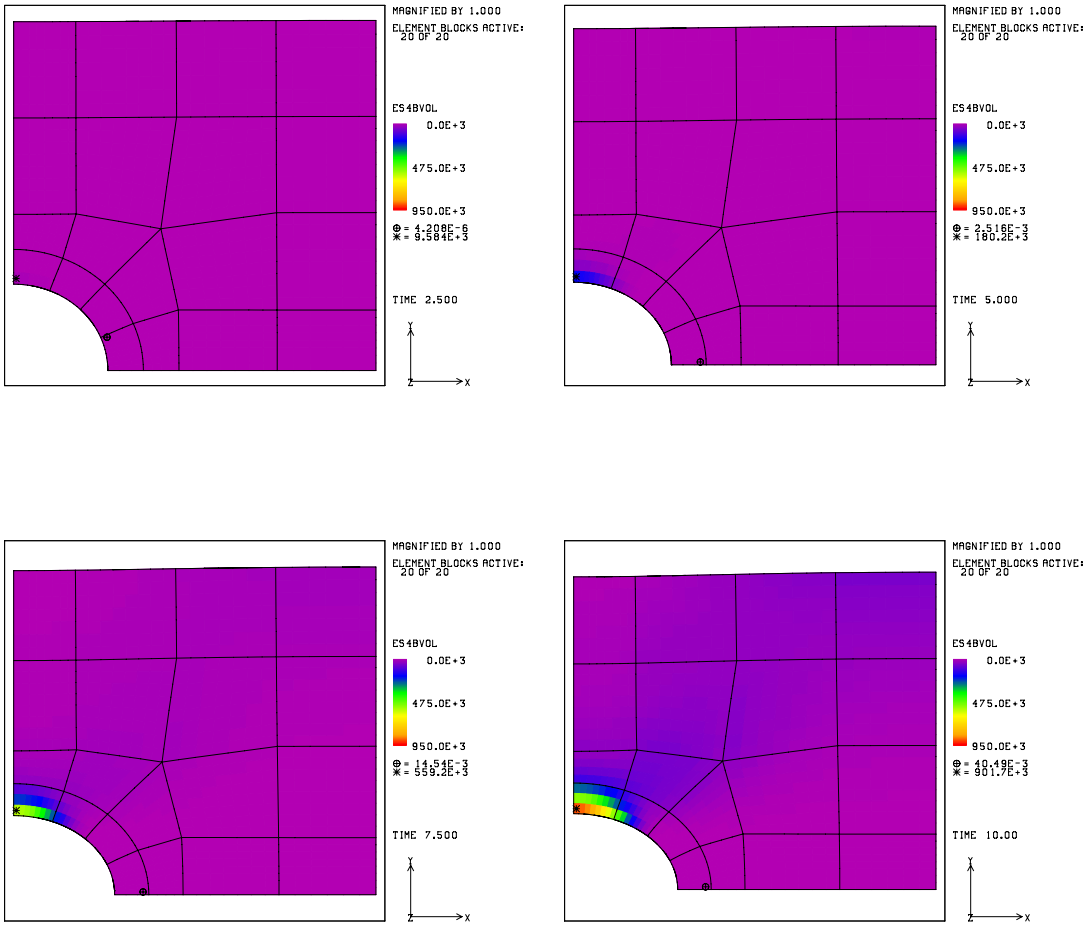

Figure 4: Contribution of each element to ζ^2 at $t = 2.5$, 5.0, 7.5 and 10 seconds (left to right, top to bottom) for the case where the WLF model (2B) is used for all elements throughout the entire analysis. Here ζ^2 compares the WLF (2B) and configurational energy (4B) models.

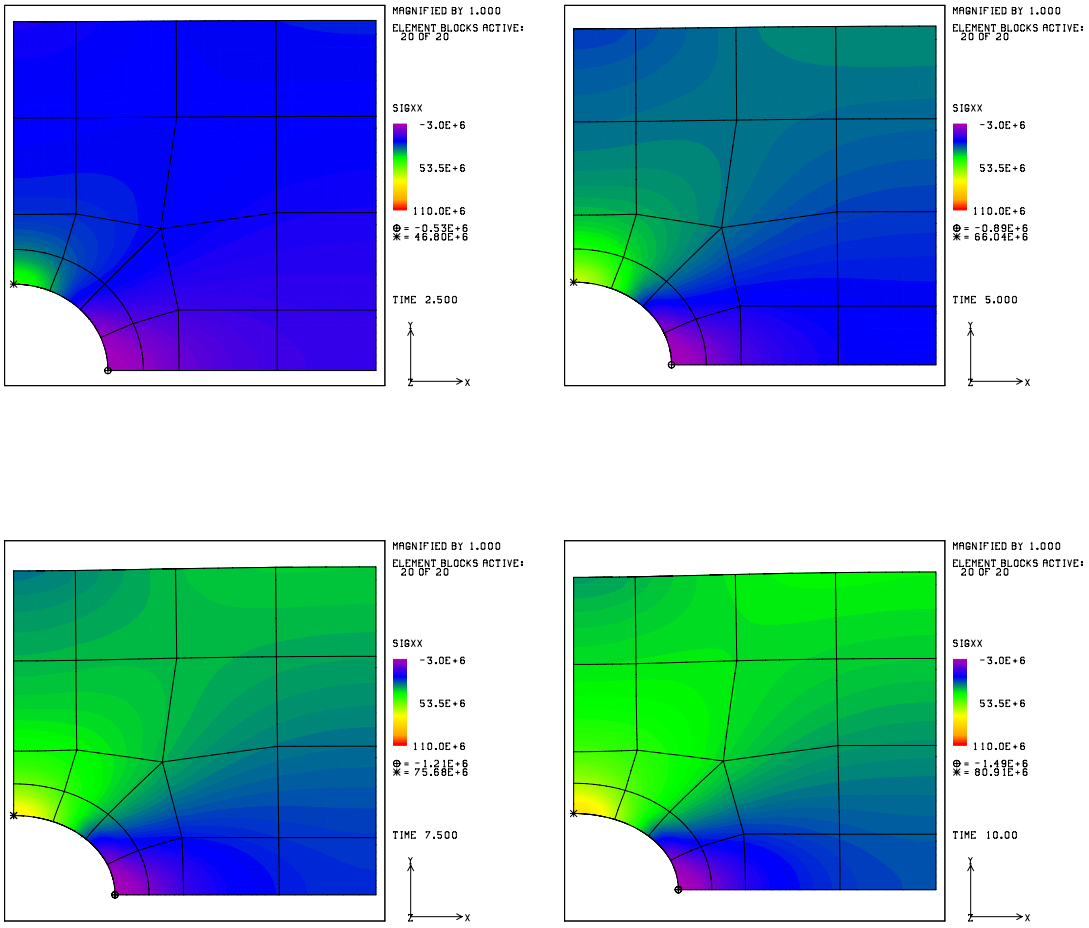

Figure 5: Cauchy stress σ_{xx} at $t = 2.5$, 5.0, 7.5 and 10 seconds (left to right, top to bottom) for the case where the configurational entropy model (3B) is used for all calculations.

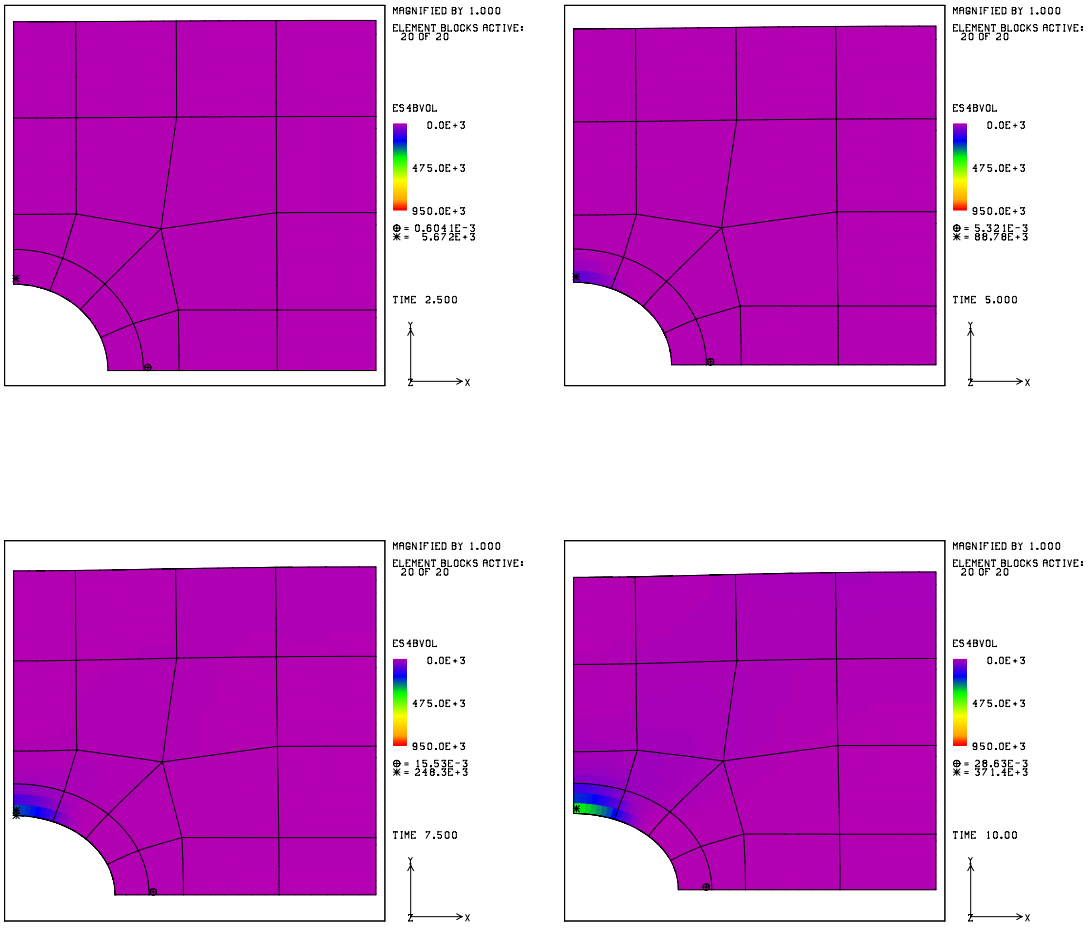

Figure 6: Contribution of each element to ζ^2 at $t = 2.5$, 5.0, 7.5 and 10 seconds (left to right, top to bottom) for the case where the configurational entropy model (3B) is used for all elements throughout the entire analysis. Here ζ^2 compares the configurational entropy (3B) and configurational energy (4B) models.

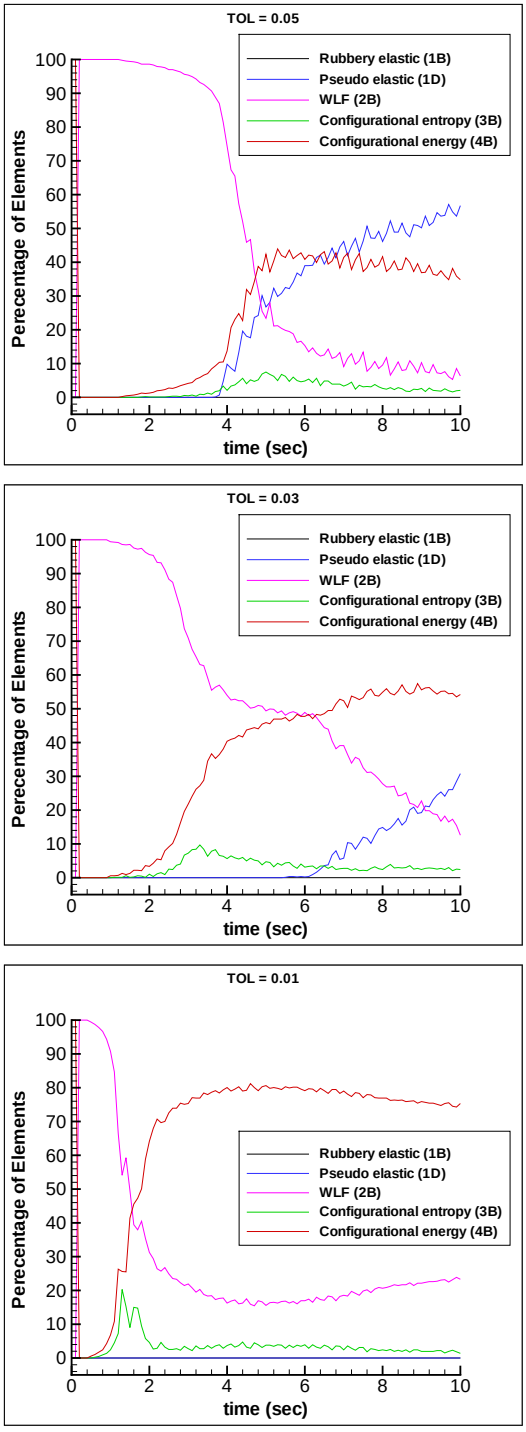

Figure 7: Time history of the models used for the case where the adaptive tolerance is 0.05, 0.03 and 0.01 (from top to bottom).

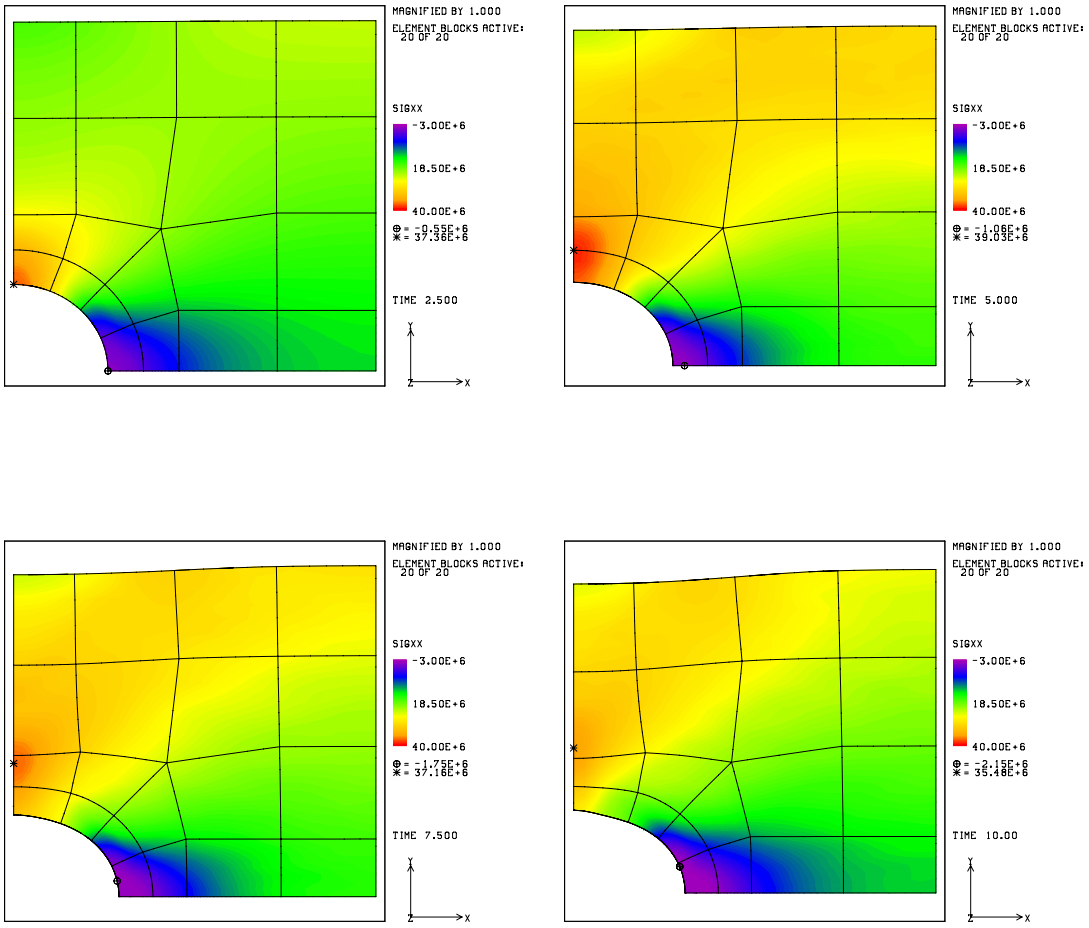

Figure 8: Cauchy stress σ_{xx} at $t = 2.5$, 5.0, 7.5 and 10 seconds (left to right, top to bottom) for the case where the adaptive tolerance level is 0.05.

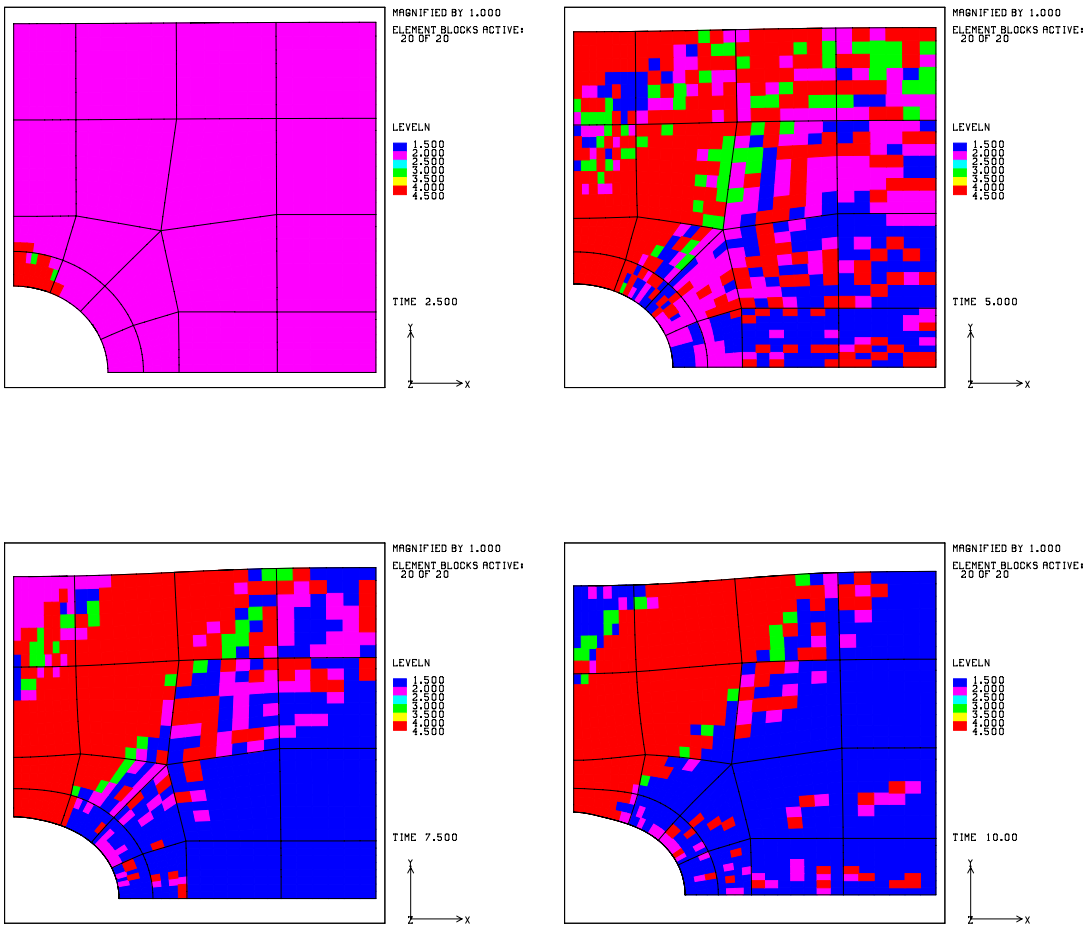

Figure 9: Models used for the time steps ending at $t = 2.5$, 5.0, 7.5 and 10 seconds (left to right, top to bottom) for the case where the adaptive error tolerance is 0.05 (configurational energy (4B) = red, configurational entropy (3B) = green, WLF (2B) = purple, pseudo elastic (1D) = blue).

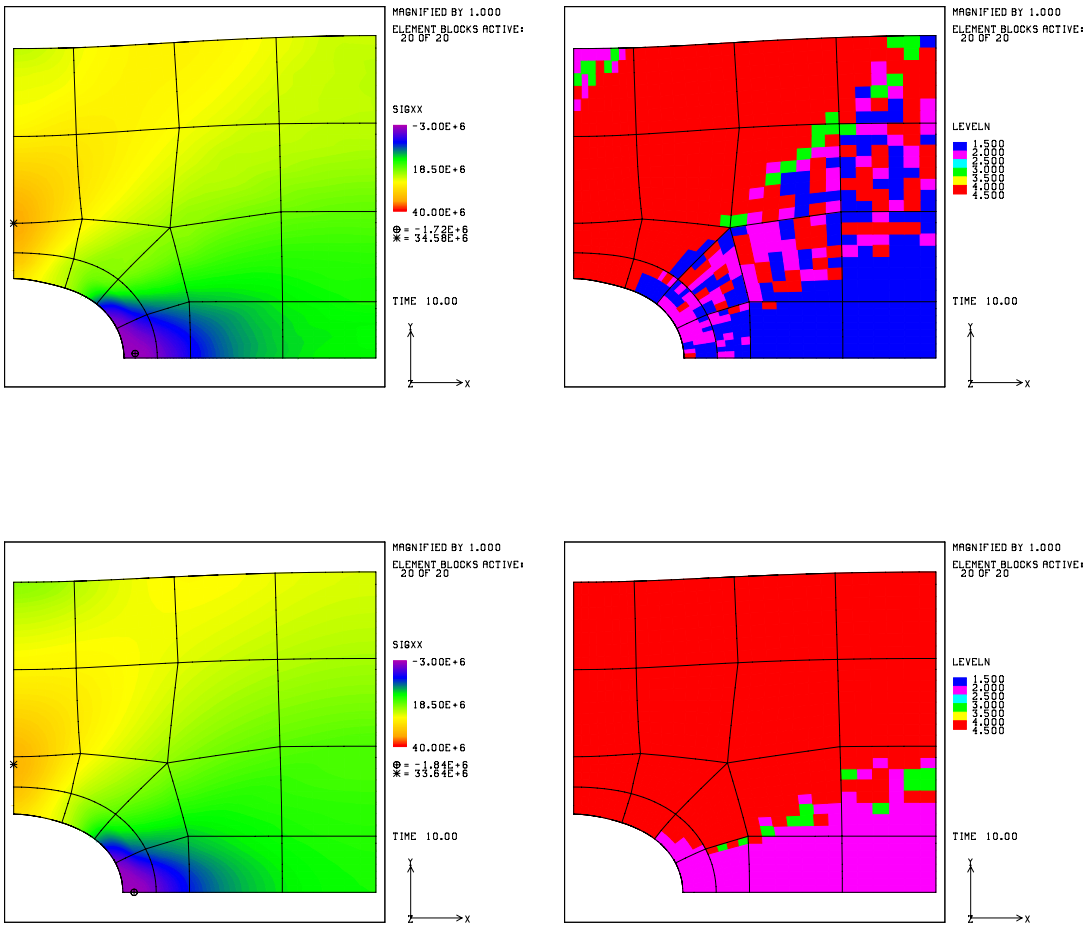

Figure 10: Cauchy stress σ_{xx} at 10.0 sec (left) and the models used over the time step ending at 10.0 sec (right) (configurational energy (4B) = red, configurational entropy (3B) = green, WLF (2B) = purple, pseudo elastic (1D) = blue) for the case where the adaptive error tolerance is 0.03 (top) and 0.01 (bottom).

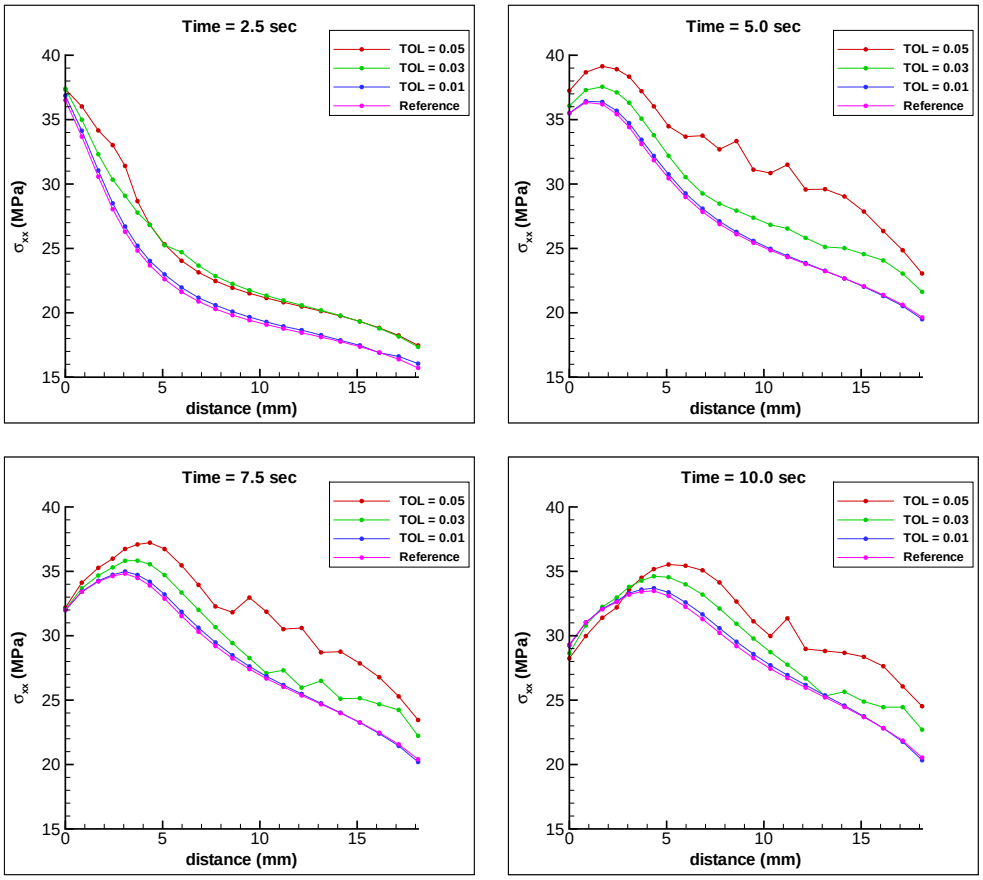

Figure 11: Cauchy stress σ_{xx} along path A at discrete times. The adaptive solutions using three tolerance levels along with the reference solution computed using the configurational energy model (4B) for all times are shown.

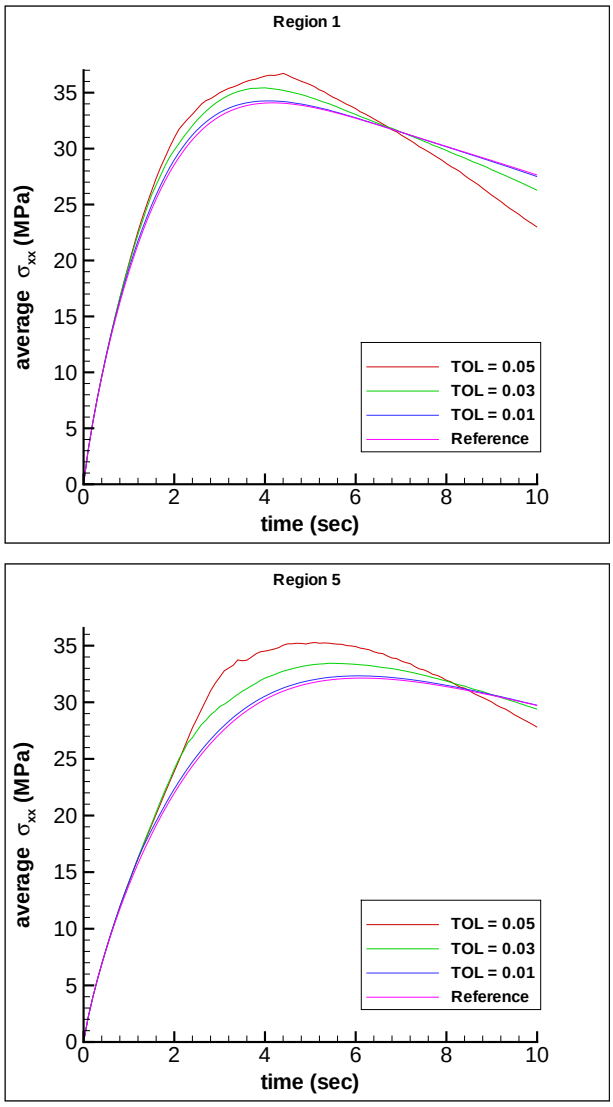

Figure 12: Average Cauchy stress σ_{xx} over region 1 (top) and region 5 (bottom). The adaptive solutions using three tolerance levels along with the reference solution are shown.

Appendix

A.1 Nonlinear Viscoelastic (NLVE) Family of Material Models

In rational mechanics, expressions for the stress, entropy and internal energy are determined from the expression for the specific Helmholtz free energy ψ (J/g) which is given in a generalized Lamé constant form for the nonlinear viscoelastic family presently being examined as follows:

$$\begin{aligned}\psi(t) &= \psi^{\infty}(t) + \Delta G_0^1 \sum_{i=1}^{N} g_i^1 (\boldsymbol{I}_{\mathcal{C}}^i(t) : \boldsymbol{I})^2 + \Delta G_0^2 \sum_{i=1}^{N} g_i^2 (\boldsymbol{I}_{\mathcal{C}}^i(t) : \boldsymbol{I}_{\mathcal{C}}^i(t)) \\ &\quad + \Delta A_0 \sum_{i=1}^{N} a_i (\boldsymbol{I}_{\mathcal{C}}^i(t) : \boldsymbol{I}) I_{\theta}^i(t) + \Delta C \sum_{i=1}^{N} c_i (I_{\theta}^i(t))^2 \end{aligned} \tag{A.1}$$

where $\boldsymbol{I}_{\mathcal{C}}^i$ and I_{θ}^i are state variables that represent integral histories of strain and temperature, respectively. Furthermore in Eq. (A.1), $\Delta(\cdot)$ denotes $(\cdot)^g - (\cdot)^{\infty}$ (i.e., the difference between the glassy and rubbery value of a relaxation modulus) and these coefficients have been taken to be constant. Also, all four relaxation spectra have been expressed as Prony series with identical distributions of relaxation times. The quantity $\boldsymbol{I}_{\mathcal{C}}^i(t)$ is given by

$$\boldsymbol{I}_{\mathcal{C}}^i(t) = \int_{-\infty}^{t} \exp\left[-\frac{(t^* - \xi^*)}{\tau_i}\right] \frac{d\boldsymbol{\mathcal{C}}}{d\xi}\, d\xi \tag{A.2}$$

where $t^* - \xi^*$ represents a difference in the reduced or material time scale, τ_i is the i^{th} relaxation time and $\boldsymbol{\mathcal{C}}$ is the Hencky strain measure given by

$$\boldsymbol{\mathcal{C}} = \boldsymbol{I} + \ln \boldsymbol{C} \tag{A.3}$$

and $\boldsymbol{C}$ is the right Cauchy-Green strain tensor given by

$$\boldsymbol{C} = \boldsymbol{F}^T \boldsymbol{F} \tag{A.4}$$

Similarly, $I_{\theta}^i(t)$ is given by

$$I_{\theta}^i(t) = \int_{-\infty}^{t} \exp\left[-\frac{(t^* - \xi^*)}{\tau_i}\right] \frac{d\theta}{d\xi}\, d\xi \tag{A.5}$$

The reduced and physical time scales are related as follows:

$$t^* - \xi^* = \int_{\xi}^{t} \frac{1}{a(u)}\, du \tag{A.6}$$

where a is the shift factor which differs in each member of the NLVE family.

The stress, entropy and the rate of entropy production are determined from

$$\frac{d\psi}{dt} = \frac{1}{\rho}\boldsymbol{P}_H : \frac{d\boldsymbol{\mathcal{C}}}{dt} - \eta\frac{d\theta}{dt} + \dot{\sigma} \tag{A.7}$$

where η is the specific entropy, $\boldsymbol{P}_H$ is the stress that is work conjugate with the Hencky strain measure and $\dot{\sigma}$ is the rate of entropy generation. The Hencky stress is found to be

$$\frac{1}{2\rho_g}\boldsymbol{P}_H = \frac{1}{2\rho_g}\boldsymbol{P}_H^{\infty} + 2\Delta G_0^1 \sum_{i=1}^{N} g_i^1 (\boldsymbol{I}_{\mathcal{C}}^i : \boldsymbol{I})\boldsymbol{I} + 2\Delta G_0^2 \sum_{i=1}^{N} g_i^2\, \boldsymbol{I}_{\mathcal{C}}^i + \Delta A_0 \sum_{i=1}^{N} a_i I_\theta^i\, \boldsymbol{I} \tag{A.8}$$

where ρ_g is the reference density in a stress free state at the glass transition temperature θ_g. The equilibrium contribution to the Hencky stress is as follows:

$$\boldsymbol{P}_H^{\infty} = \left[4\rho_g \left(G_0^1\right)^{\infty} (\boldsymbol{\mathcal{C}} : \boldsymbol{I} - 3) + 2\rho_g A_0^{\infty}(\theta - \theta_g)\right] \boldsymbol{I} + 4\rho_g \left(G_0^2\right)^{\infty} (\boldsymbol{\mathcal{C}} - \boldsymbol{I}) \tag{A.9}$$

The second Piola Kirchhoff stress tensor is given in terms of the Hencky stress tensor by the following relationship:

$$\boldsymbol{P} = \boldsymbol{P}_H : \frac{d\boldsymbol{\mathcal{C}}}{d\boldsymbol{C}} \tag{A.10}$$

A.2 Configurational Energy Model

The most sophisticated and, hence, accurate member of the NLVE family of material models uses a shift factor based on a quantity termed the configurational internal energy. Briefly, the configurational internal energy E_c is the internal energy of the actual viscoelastic material minus that coming from its glassy response to the same volumetric and thermal history. Recall that the specific internal energy E is as follows:

$$E = \psi + \theta\eta \tag{A.11}$$

The current value of the configurational energy E_c depends on the current values of $\boldsymbol{I}_{\mathcal{C}}^i$ and I_θ^i. Then, the shift factor in terms of the configurational energy is

$$\log_{10}[a] = B\left(\frac{1}{E_c} - \frac{1}{\Delta_{ref}}\right) \tag{A.12}$$

where B is a constant in the present work. Using a shift factor which depends upon the configurational internal energy gives a material clock which depends upon the thermal, volumetric strain and stress histories through $\boldsymbol{I}_{\mathcal{C}}^i$ and I_θ^i.

The quasi-static equilibrium states are determined at discrete times in the finite element solution with numerical integration used for the constitutive equation. The history integrals in this model and all other models except for the two elastic models to be defined later are marched in time using a modified central difference scheme [3, 4] as follows:

$$\boldsymbol{I}^i_{\mathcal{C}}(t^n) = \left(\frac{2a_{avg}\tau_i - \Delta t_{min}}{2a_{avg}\tau_i + \Delta t_{min}}\right)\boldsymbol{I}^i_{\mathcal{C}}(t^{n-1}) + \left(\frac{2a_{avg}\tau_i \Delta t_{min}}{2a_{avg}\tau_i + \Delta t_{min}}\right)\left(\frac{\boldsymbol{\mathcal{C}}(t^n) - \boldsymbol{\mathcal{C}}(t^{n-1})}{\Delta t^n}\right) \tag{A.13}$$

and

$$I^i_{\theta}(t^n) = \left(\frac{2a_{avg}\tau_i - \Delta t_{min}}{2a_{avg}\tau_i + \Delta t_{min}}\right)I^i_{\theta}(t^{n-1}) + \left(\frac{2a_{avg}\tau_i \Delta t_{min}}{2a_{avg}\tau_i + \Delta t_{min}}\right)\left(\frac{\theta(t^n) - \theta(t^{n-1})}{\Delta t^n}\right) \tag{A.14}$$

where

$$\Delta t_{min} = \min\left\{\Delta t^n, 2a_{avg}\tau_i\right\} \tag{A.15}$$

For the configurational energy model (4B), a_{avg} is given by

$$\log_{10}[a_{avg}] = B\left(\frac{2}{E_c(t^n) + E_c(t^{n-1})} - \frac{1}{\Delta_{ref}}\right) \tag{A.16}$$

A simple fixed point iteration scheme is used to converge the nonlinear constitutive calculations given $\boldsymbol{\mathcal{C}}(t^{n-1})$, $\boldsymbol{\mathcal{C}}(t^n)$, $J(t^n)$, $\theta(t^{n-1})$, $\theta(t^n)$, $\boldsymbol{I}^i_{\mathcal{C}}(t^{n-1})$, $I^i_{\theta}(t^{n-1})$ and $E_c(t^{n-1})$ where $J = \det \boldsymbol{F}$.

A.3 Configurational Entropy Model

Similar to the configurational internal energy, the configurational internal entropy is defined as that coming from the actual specimen minus the internal entropy from the specimen's glassy response under the same volumetric strain and thermal histories. Noting Eq. (A.11), it should be apparent that the configurational internal energy contains terms corresponding to the configurational entropy. In order to be consistent with the configurational energy model, the shift factor in the configurational entropy model (3B) is actually based on $\theta_g \eta_c$ where η_c is the actual configurational entropy. For this coarse model, $\log_{10}[a]$ is written as

$$\log_{10}[a] = B\left(\frac{1}{\theta_g \eta_c} - \frac{1}{\Delta_{ref}}\right) \tag{A.17}$$

For the numerical integration, a_{avg} is determined from

$$\log_{10}[a_{avg}] = B\left(\frac{2}{\theta_g\eta_c(t^n) + \theta_g\eta_c(t^{n-1})} - \frac{1}{\Delta_{ref}}\right) \tag{A.18}$$

Similar to the configurational energy model (4B), a fixed point integration scheme is used to converge the nonlinear constitutive calculations that result from η_c being a function of $\boldsymbol{I}_C^i$ and I_θ^i. The configurational entropy model (3B) includes the effects of the volumetric strain and thermal histories on $\log_{10}[a]$ and is a good approximation to the configurational energy model (4B) for the case where the stresses are at or below moderate levels.

A.4 WLF Model

For the case of a polymer subjected to low to moderate stresses when the polymer is at temperatures ranging from θ_g to approximately $\theta_g + 100\,\mathrm{K}$, wide experimental evidence indicates that $\log_{10}[a]$ can be expressed strictly in terms of the current temperature by the well-known Williams-Landel-Ferry [1] relationship which is given as follows:

$$\log_{10}[a] = \frac{-C_1(\theta - \theta_g)}{C_2 + (\theta - \theta_g)} \tag{A.19}$$

where C_1 and C_2 are material constants. Because the horizontal shift factor in this case depends only on the temperature and not on the stress or strain, it is properly termed a thermorheologically simple linear viscoelastic model. Of course, the material response is nonlinear in terms of the thermal history. It should also be noted that the proper kinematics for large deformations/strains are still used in this and all other models. For the numerical integration of the constitutive law, a_{avg} is determined using Eq. (A.19) with θ replaced by $\theta_{avg} = [\theta(t^n) + \theta(t^{n-1})]/2$. Because temperature is assumed to be specified, no iterations are required for the material law calculations in this model.

A.5 Elastic Models

The material response of a cross-linked polymer at very short or very long elapsed times since a load was applied can be characterized elastically using the appropriate constants that describe the polymer's glassy and rubbery moduli. That is, it is not

necessary to consider any material relaxations in order to find the initial and final viscoelastic response of the material. For such a glassy response, essentially no material relaxations have had a chance to occur since the load was applied, whereas for the corresponding rubbery response, all material relaxations have been completed since the load was applied. Furthermore, these glassy or rubbery moduli could be used to determine the initial or final viscoelastic structural responses for all path-independent problems, respectively. The idea of not computing any material relaxations will be generalized into two elastic models which can be used in combination with the previously presented viscoelastic models in computing the nonlinear, possibly path-dependent, structural responses for structures composed of materials falling into the NLVE family. The pseudo elastic model (1D) that will be defined corresponds to the case where all material relaxations are proceeding extremely slowly over each time step in which the model is used, whereas the rubbery elastic model (1B) will give the result for the case where all relaxations have reached completion by the end of the time step in which it is used. Because neither model includes the explicit use of a shift factor a, no iterations are required to converge the numerical computation of either constitutive model.

A.5.1 Pseudo Elastic Model

For the pseudo elastic response over the current time step, consider the following exact equation for $I_\theta^i(t^n)$:

$$I_\theta^i(t^n) = \exp\left[-\frac{(\Delta t^*)^n}{\tau_i}\right] I_\theta^i(t^{n-1}) + \int_{t^{n-1}}^{t^n} \exp\left[-\frac{(t^*)^n - \xi^*}{\tau_i}\right] \frac{d\theta}{d\xi}\, d\xi \tag{A.20}$$

For this model, the assumption is that t^* changes very little over the current time step so that the following approximation for $I_\theta^i(t^n)$ is acceptable:

$$I_\theta^i(t^n) \approx I_\theta^i(t^{n-1}) + \theta(t^n) - \theta(t^{n-1}) \tag{A.21}$$

Likewise, $\boldsymbol{I}_{\mathcal{C}}^i(t^n)$ is updated using

$$\boldsymbol{I}_{\mathcal{C}}^i(t^n) = \boldsymbol{I}_{\mathcal{C}}^i(t^{n-1}) + \boldsymbol{\mathcal{C}}(t^n) - \boldsymbol{\mathcal{C}}(t^{n-1}) \tag{A.22}$$

It should be apparent from Eq. (A.6) that small Δt^* over a time step results from Δt being very small and/or $\log_{10}[a]$ tending to be positive and relatively large over the

time step. Note that if other models in the NLVE family have been used before the pseudo elastic approximation (1D), the pseudo elastic (1D) results will not correspond simply to using $\boldsymbol{P}_H = \boldsymbol{P}_H^\infty$ with the rubbery moduli replaced by the corresponding glassy values in Eq. (A.9). However, if only this model has been used for all times over a given region, then the Hencky stress for that region would be $\boldsymbol{P}_H = \boldsymbol{P}_H^\infty$ with the rubbery moduli replaced by the corresponding glassy values. That is, using the pseudo elastic model for all time steps gives purely a glassy elastic response. Regardless of what other models may have been used in previous time steps, the response of this model to any load increments applied in the current time step is the traditional glassy elastic response of the polymer. Hence, this model can be thought of as an enhanced glassy elastic model that can also be used in time steps where Δt^* is small.

A.5.2 Rubbery Elastic Model

For the rubbery elastic model (1B), all material relaxations which started before and during the current time step are assumed to reach completion by the end of the current time step. For this to be true, the elapsed reduced time since any loading was applied needs to be relatively large. Exactly how large this is can be determined from the largest relaxation time appearing in the Prony series that are used to characterize the viscoelastic material. A large amount of elapsed reduced time since a load was applied may or may not correspond to a large amount of elapsed physical time. Recall that the reduced and physical time scales are related as given by Eq. (A.6). For instance, if $\log_{10}[a]$ is constant at -2, the rate at which the reduced time proceeds would be two orders of magnitude larger than the rate at which physical time elapses. Because all relaxations are assumed to be completed by the end of the time step, all integral histories $\boldsymbol{I}_{\mathcal{C}}^i$ and I_θ^i are set to zero, while the Hencky stress at the end of the time step is simply $\boldsymbol{P}_H^\infty$ as given by Eq. (A.9).

A.6 Hierarchy of NLVE Material Models

The adaptive scheme will allow individual elements or groups of elements to use the model requiring the minimum computational effort over each time step while still achieving the necessary accuracy. In terms of least to largest amount of computational cost, the models are ordered as rubbery elastic (1B), pseudo elastic (1D), WLF (2B),

configurational entropy (3B), and configurational energy (4B). In terms of the physics captured in $\log_{10}[a]$, the non-elastic models are ordered as WLF (2B), configurational entropy (3B), and configurational energy (4B). Discounting any possible pathological examples, if the WLF model (2B) is accurate, then so is the configurational entropy model (3B). Although they do not compute what the actual viscoelastic relaxations are over a given time step, either of the two elastic models may be accurate over certain time steps for a given loading scenario. As the most detailed model in the NLVE family, the configurational energy model (4B) is assumed to capture all of the relevant physics. Hence, the assessment of accuracy of any of the coarse NLVE models must be made with respect to the configurational energy model (4B).

References

[1] J. J. Aklonis and W. J. MacKnight. *Introduction to Polymer Viscoelasticity*. Wiley, New York, 2nd edition, 1983.

[2] M. L. Blanford. Jas3d: A multi-strategy iterative code for solid mechanics analysis. Sandia National Laboratories, 1998.

[3] R. S. Chambers. The numerical integration and 3-d finite element formulation of a viscoelastic model of glass. SAND94-1607, Sandia National Laboratories, 1994.

[4] R. S. Chambers, D. B. Adolf, and J. M. Caruthers. A comprehensively validated theory of the nonlinear viscoelasticity of glassy polymers. In preparation.

[5] J. R. Cho and J. T. Oden. A priori modeling error estimates of hierarchical models for elasticity problems for plate- and shell-like structures. *Mathematics of Computer Modeling*, 23(10):117–133, 1996.

[6] J. R. Cho and J. T. Oden. Local a posteriori error estimation of hierarchical models for plate- and shell-like structures. *Computers in Mathematics with Applications*, 149:33–48, 1997.

[7] P. G. Ciarlet. *Mathematical Elasticity, Volume 1: Three Dimensional Elasticity*, volume 20 of *Stud. Math. and Appl.* North-Holland, Amsterdam, 1988.

[8] N. Moës, J. T. Oden, and K. Vemaganti. A two-scale strategy and a posteriori error estimation for modeling heterogeneous structures. In P. Ladevèze and J. T. Oden, editors, *Advances in Adaptive Computational Methods in Mechanics*, volume 47 of *Stud. Appl. Mech.*, pages 115–133. Elsevier, Amsterdam, 1998.

[9] N. Moës, J. T. Oden, K. Vemaganti, and J.-F. Remacle. Simplified methods and a posteriori error estimation for the homogenization of representative volume elements (RVE). *Comput. Methods Appl. Mech. Engrg.*, 176:265–278., 1999.

[10] J. T. Oden and J. R. Cho. Adaptive hpq-finite element methods of hierarchical models for plate-and shell-like structures. *Comput. Methods Appl. Mech. Engrg.*, 136(3-4):317–346, 1996.

[11] J. T. Oden and K. Vemaganti. Adaptive hierarchical modeling of heterogeneous structures. predictability: quantifying uncertainty in models of complex phenomena. *Phys. D*, 133:404–415, 1999.

[12] J. T. Oden and K. Vemaganti. Estimation of local modeling error and goal-oriented modeling of heterogeneous materials; Part I: error estimates and adaptive algorithms. *Journal of Computational Physics*, To appear.

[13] P. J. Roache. *Verification and Validation in Computational Science and Engineering*. Hermosa, Albuquerque, NM, 1998.

[14] K. Vemaganti and J. T. Oden. Estimation of local modeling error and goal-oriented modeling of heterogeneous materials; Part II: A computational environment for adaptive modeling of heterogeneous elastic solids. In preparation.

DISTRIBUTION:

2 TICAM
The University of Texas at Austin
Attn: J. T. Oden
S. Prudhomme
201 E. 24th Street, ACE 6.412
Austin, TX 78712

1 Poznan University of Technology
Attn: Mieczyslaw S. Kuczma
5 Maria Sk^{3}odowska-Curie Sq.
60-965 Poznan, Poland

1	MS 0310	P. Yarrington, 9230
1	MS 0316	S.S. Dosanjh, 9233
1		G.S. Heffelfinger, 9235
1	MS 0318	G.S. Davidson, 9212
1		P.D. Heermann, 9227
1	MS 0321	W.J. Camp, 9200
1		A.L. Hale, 9220
1	MS 0555	M.S. Garrett, 9122
1	MS 0557	T.J. Baca, 9125
1	MS 0819	E.A. Boucheron, 9231
1		K.H. Brown, 9231
1	MS 0820	P.F. Chavez, 9232
1	MS 0825	W.H. Rutledge, 9115
1	MS 0826	W.L. Hermina, 9113
1		J.R. Stewart, 9131
1	MS 0827	J.D. Zepper, 9131
1	MS 0828	J.L. Moya, 9132
1		M. Pilch, 9133

1	MS 0834	J.E. Johannes, 9114
1		A.C. Ratzel, 9110
1	MS 0835	S.N. Kempka, 9111
1		J.S. Peery, 9121
1	MS 0836	R.O. Griffith, 9117
1		E.S. Hertel, 9116
1		J.M. McGlaun, 5903
1	MS 0841	T.C. Bickel, 9100
1	MS 0847	S.W. Attaway, 9121
1		M.L. Blanford, 9121
1		R.S. Chambers, 9123
1		A.F. Fossum, 9123
30		D.C. Hammerand, 9123
1		M.W. Heinstein, 9121
1		J. Jung, 9132
1		S.W. Key, 9121
1		R.W. Leland, 9226
1		C.S. Lo, 9123
1		D.R. Martinez, 9124
1		R.A. May, 9126
1		J.A. Mitchell, 9121
1		H.S. Morgan, 9120
1		D.J. Segalman, 9124
1		W.M. Scherzinger, 9123
1		C.M. Stone, 9121
1		G.W. Wellman, 9123
1	MS 0888	D.B. Adolf, 1811
1	MS 9042	J.L. Handrock, 8727
1	MS 9161	E.P. Chen, 8726

1	MS 9405	D.J. Bammann, 8726
1		M.F. Horstemeyer, 8726
1		R.E. Jones, 8726
1		R.A. Regueiro, 8726
1	MS 1110	L.G. Benavides, 9213
1		N.D. Pundit, 9223
1		D.E. Womble, 9214
1	MS 1135	J.T. Nakos, 9134
1	MS 0188	Laboratory Directed Research & Development
1	MS 9018	Central Technical Files, 8945-1
2	MS 0899	Technical Library, 9616
1	MS 0612	Review & Approval Desk, 9612 For DOE/OSTI